JGR Atmospheres

RESEARCH ARTICLE
10.1029/2020JD032465

Special Section:
Southern Ocean clouds, aerosols, precipitation and radiation

Key Points:
- Marine cold air outbreak parameter M correlates better with low-level cloud boundaries than other stability measures in midlatitudes
- Differences in large-scale conditions at Northern and Southern Hemisphere sites explain differences in sensitivities to M
- A general circulation model reproduces similar relationships, but sensitivities differ causing cooler clouds than observed for a given M

Supporting Information:
- Supporting Information S1

Correspondence to:
C. M. Naud,
catherine.naud@columbia.edu

Citation:
Naud, C. M., Booth, J. F., Lamer, K., Marchand, R., Protat, A., & McFarquhar, G. M. (2020). On the relationship between the marine cold air outbreak M parameter and low-level cloud heights in the midlatitudes. *Journal of Geophysical Research: Atmospheres*, *125*, e2020JD032465. https://doi.org/10.1029/2020JD032465

Received 17 JAN 2020
Accepted 6 MAY 2020
Accepted article online 15 MAY 2020

©2020. American Geophysical Union. All Rights Reserved.

On the Relationship Between the Marine Cold Air Outbreak M Parameter and Low-Level Cloud Heights in the Midlatitudes

Catherine M. Naud[1], James F. Booth[2], Katia Lamer[2], Roger Marchand[3], Alain Protat[4], and Greg M. McFarquhar[5]

[1]Applied Physics and Applied Mathematics, Columbia University/NASA-GISS, New York, NY, USA, [2]Earth and Atmospheric Sciences, CUNY-City College, New York, NY, USA, [3]JISAO, University of Washington, Seattle, WA, USA, [4]Australian Bureau of Meteorology, Melbourne, Victoria, Australia, [5]School of Meteorology and Cooperative Institute for Mesoscale Meteorology Studies (CIMMS), University of Oklahoma, Norman, OK, USA

Abstract Focusing on conditions of subsidence when low clouds are present, ground-based observations in both the North Atlantic and the Southern Ocean reveal strong relationships between cloud boundary (base and top heights) and different measures of lower tropospheric instability. The difference in potential temperature between the surface and 800 hPa (a metric called M) provides a stronger relationship than measures of inversion strength such as the lower tropospheric stability and estimated inversion strength. This is because (1) inversion strength itself does not correlate well with cloud boundaries, and (2) M contains information that appears important for cloud boundaries. These include the surface forcing through the use of sea surface rather than near-surface air temperature and an upper level close to the real cloud top. These results expand upon previous work on the importance of M as a predictor of cloud morphology. However, important differences are found in low-cloud conditions for the North Atlantic as compared to the Southern Ocean (for a given value of M): stronger inversions, deeper boundary layers, and much larger sea level pressures. Therefore, the relationship between cloud boundaries and M differs between the two regions. A general circulation model provides similar relationships as observed between M and both cloud top height and temperature but tends to place clouds higher and at colder temperatures than observed for a given M. This might cause issues with the representation of precipitation, cloud cover and radiation in the Southern Ocean.

1. Introduction

Over the extratropical oceans, boundary layer clouds dominate (Mace et al., 2009), and because they have a net cooling effect, they are an important component of the radiation budget (e.g., Hartmann et al., 1992; Haynes et al., 2011). The response of these clouds to changes in climate forcing remains a critical and open question (e.g., Eastman et al., 2011; Schneider et al., 2019; Zelinka et al., 2020). The formation of stratocumulus clouds is driven by radiative cooling at cloud top and convective instability in the boundary layer. The associated large-scale conditions typically feature subsidence and stable conditions aloft that help promote a strong inversion and radiative cooling. However, once formed, as long as subsidence strength does not increase (Myers & Norris, 2013), these clouds can persist in situations with little boundary layer instability such that the stratocumulus layer becomes decoupled from the surface (Wood, 2012, and references therein). Thus, the representation of these clouds in models is strongly dependent on the correct representation of shallow convection and the boundary layer structure. At the current horizontal and vertical resolution of climate models, the majority of convection and boundary layer processes need to be parameterized. A number of large-scale parameters have been proposed to help predict the properties of oceanic stratiform low clouds (e.g., Klein et al., 2017; Klein & Hartmann, 1993; Kuo & Schubert, 1988; Wood & Bretherton, 2006, and references therein), with the objective of either evaluating (e.g Kelleher & Grise, 2019) or improving model parameterizations (e.g., Köhler et al., 2011; Zhao et al., 2018). While the cloud property that dominates these studies is cloud fraction (CF), which is important for the accurate representation of their radiative forcing, other measures can help inform on cloud type and their representation in models. We focus here on cloud boundaries, which are critical to the correct representation of low clouds in models and ultimately impact their optical and microphysical characteristics (effective particle size).

Using the difference in potential temperature between 700 hPa and the surface as a measure of lower tropospheric stability (LTS), Klein and Hartmann (1993) showed that LTS correlates well with low-level CF in subtropical regions with frequent occurrence of oceanic stratocumuli. In part because of limitations with LTS in the extratropics, this measure was refined with the introduction by Wood and Bretherton (2006) of the estimated inversion strength (EIS), which takes advantage of the fact that the temperature profile between the lifting condensation level (LCL) (cloud base) and 700 hPa is often close to that of a moist adiabat. EIS was found to work equally well in the subtropics and extratropics as a predictor of CF (e.g., Kawai et al., 2017). Both LTS and EIS were originally tested in relatively quiescent dynamical conditions (Wood & Bretherton, 2006 impose a moderate subsidence rate at 850 hPa in the range 0.2–0.8 cm s^{-1}), as is often the case in subtropical regions (e.g., Myers & Norris, 2013). However, EIS was found to still be well correlated with CF in extratropical cyclones, more specifically in the wake of the cold fronts where subsidence is strong and stratiform clouds ubiquitous (Naud et al., 2016). Furthermore, EIS was also found to be a good predictor of cloud base and top height, but another measure of LTS, a marine cold air outbreak (MCAO) index, M (Fletcher et al., 2016a), is a better predictor (Lamer et al., 2020; Naud et al., 2018).

The MCAO index M is defined as the difference in potential temperature between the surface and 800 hPa. This parameter relies on dry variables (similar to LTS), and its better performance for cloud boundaries (i.e., base and top heights and top temperature) compared to EIS is intriguing. The Naud et al. and Lamer et al. studies are based solely on observations acquired at the Department of Energy Atmospheric Radiation Measurement (ARM) Eastern North Atlantic (ENA) site, situated in the Azores Archipelago, a region dominated by anticyclonic conditions (e.g., Rémillard et al., 2012; Wood et al., 2015). While the ENA site has been found to be representative of most low-level cloud regions (Ahlgrimm & Forbes, 2014; Rémillard & Tselioudis, 2015), the question of whether M correlates with cloud properties in other regions/conditions needs to be verified. Recently, McCoy et al. (2017) found that stratocumulus clouds organization, in particular the transition from closed to open cells, was strongly related with the M index in the extratropical oceans. This provides additional motivation to test whether the correlations between M and cloud base and top heights are found in other extratropical locations than the northeastern Atlantic.

Therefore, in this manuscript we use data collected during recent observational campaigns conducted in the Southern Ocean (SO) to (1) demonstrate that the M index is a useful predictor of cloud base and top height for SO low-level clouds as well, (2) explore why M is a better predictor than LTS and EIS, and (3) examine the applicability of these relationships for general circulation model (GCM) evaluation by performing a brief analysis of a 5-year integration of the free-running Community Atmospheric Model Version 6 (CAM6; e.g., Gettelman et al., 2018).

2. Observations and Methods

In this section, we present the data sets, the case selection method, and the stability metrics that we examine.

2.1. SO Campaigns and the ENA Site Data

A series of related measurement campaigns were organized to explore clouds and aerosols in the pristine oceanic region between Tasmania and Antarctica between 2016 and 2018. This included deployment of aircraft-, ship-, and ground-based instruments. Specifically, we use data from three of these campaigns:

1. The Clouds, Aerosols, Precipitation, Radiation and Atmospheric Composition over the SO experiment (CAPRICORN; for more details see Protat et al., 2017; Mace & Protat, 2018), conducted on board the Australian Bureau of Meteorology research vessel *Investigator* between 13 March and 15 April 2016 (CAPRICORN-1, Figure 1a) and between 11 January and 21 February 2018 (CAPRICORN-2, Figure 1b). CAPRICORN-2 was part of the Southern Ocean Clouds, Radiation, Aerosol Transport Experimental Study (SOCRATES),
2. the Measurements of Aerosols, Radiation and Clouds over the Southern Ocean (MARCUS) conducted on board the Australian ice breaker the *Aurora Australis* between October 2016 and March 2017 (Figure 1c), and
3. the Macquarie Island Cloud and Radiation Experiment (MICRE) for which observations were collected on Macquarie Island (54°S, 159°E; marked in Figure 1c) between March 2016 and April 2017.

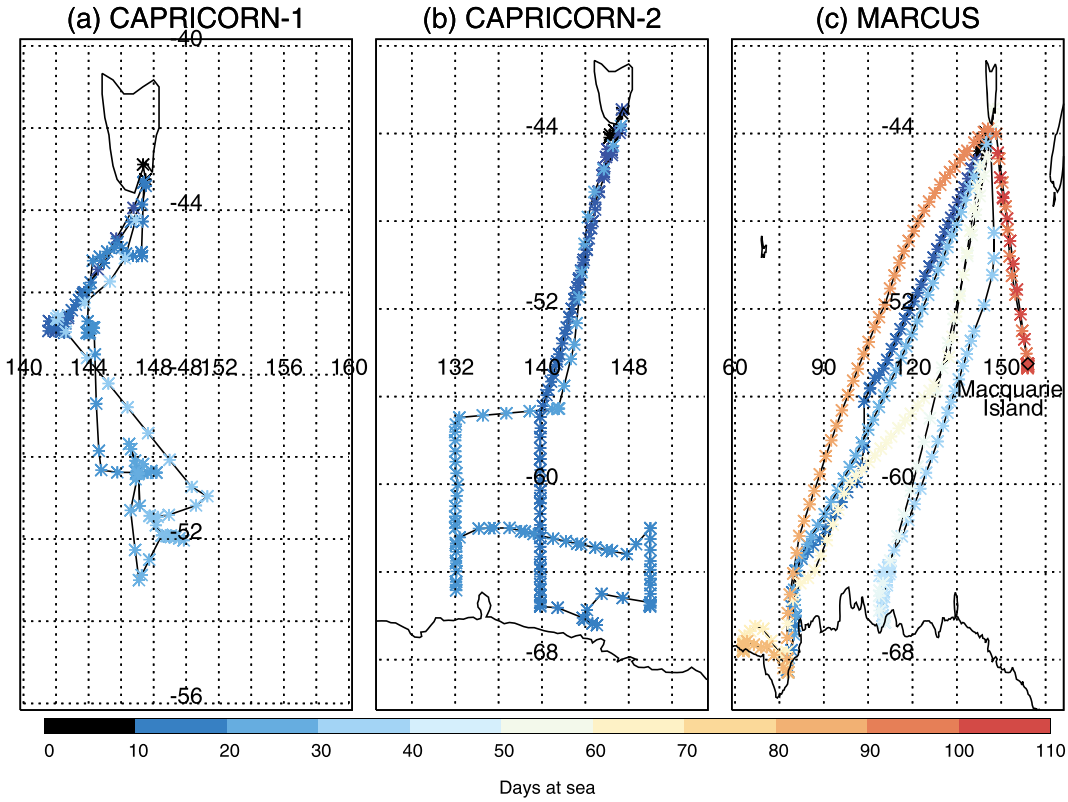

Figure 1. Maps of (a) CAPRICORN-1, (b) CAPRICORN-2, and (c) MARCUS voyages, with the location of Macquarie Island in (c). The color scale indicates the number of days at sea starting on the date of first observation.

All three campaigns collected radiosoundings (twice daily for MICRE, at least four times a day for the ship-based campaigns), surface meteorology (near-surface temperature, pressure, and relative humidity), and cloud boundaries from combined (W-band) cloud radar and lidar profiles. For CAPRICORN the radar and lidar data were collected and processed to obtain cloud base and top heights by the BoM (coauthor A. Protat), while for MICRE it was collected by BoM (A. Protat) but processed by ARM (coauthor R. Marchand). For MARCUS, they were collected and processed by ARM (Active Remote Sensing of Cloud ARSCL product, S. Giangrande and K. Johnson, ARM, 2017). All of these data sets are publically available (see Acknowledgments for details).

While measurements of sea surface temperature (SST) were conducted during the ship campaigns, they are not available for MICRE. To ensure consistency across the three campaigns, we use instead the Modern Era Reanalysis for Research Applications (MERRA-2; Gelaro et al., 2017) reanalysis 1-hourly SST and sea level pressure (SLP) to obtain the skin potential temperature (hereafter we use the term "skin" to distinguish the surface itself from the near-surface air). We note that the reanalysis, because of its coarse spatial resolution (0.625° × 0.5°), tends to provide anomalously cold temperatures south of ~66°S, presumably because of proximity to land and sea ice. We assume that this is because at these latitudes the MERRA-2 pixels are not necessarily entirely open-ocean but can include sea ice or land if close to the coastline. Consequently, we only use data from MARCUS north of 66°S (or when MERRA-2 SST is at least 271.15 K). However, we find a very good agreement between MERRA-2 and all ship-based SSTs north of 66°S within 0.1 K (Figure S1 in the supporting information). Another product that we collected from MERRA-2 is the 500-hPa vertical velocity. This product is used to indicate the conditions of subsidence (i.e., when the 500-hPa vertical velocity is positive in pressure coordinates).

In addition, for comparison with the SO data, we also collected radar-lidar combined cloud boundary retrievals (ARSCL product; ARM, 2015), radiosoundings (ARM, 1993) and meteorology information (ARM, 2013) from the ENA site (28°W, 39°N) situated on Graciosa Island in the Azores Archipelago. The same products

are collected as listed above for the SOs, and we use the same additional information from MERRA-2 to supplement the observations. The overall period of observations used here is from June 2009 to December 2010 (CAP-MBL campaign, Wood et al., 2015) and then from July 2015 to December 2018.

For all three SO campaigns and for the ENA data set, cloud base and top heights are obtained as follows: The cloud base is the first level at which the lidar detects hydrometeors (i.e., when a significant return is detected, e.g., Clothiaux et al., 1998), and the cloud top is the uppermost cloudy level below 3 km, that is detected by the radar.

2.2. Case Selection

For this analysis, we focus on data collected within 1 hr of radiosonde launches. In order to be included in the analysis, each 1-hr period containing a radiosonde launch is required to have (a) subsidence at 500 hPa (according to MERRA-2) and (b) clouds present (according to the W-band radar) with a top height below 3 km, even if this occurs for only one profile. We do not exclude multicloud layer situations where a cirrus, for example, might also be present aloft. Median cloud base and top height (based on lidar and W-band radar, respectively) during the hour are used. In contrast, the surface meteorological observations are matched in time with the radiosonde and the MERRA-2 output is selected for the hour that contains the launch time. We use the radiosonde profiles of temperature as a function of altitude to derive the cloud top temperature (CTT) at the radar-derived median cloud top height (CTH). By design, we do not examine cloud depth, even if it is radiatively more important than cloud heights. This is because in Naud et al. (2018) or more recently in Lamer et al. (2020), we did not find evidence of a relationship between stability and cloud depth. Cloud depth appears to correlate better with surface wind speed or sea-air temperature contrast, as compared to the stability metrics.

Together the CAPRICORN-1 and CAPRICORN-2 campaigns provide 75 cases that meet the imposed criteria, while MARCUS provides 125 and MICRE 179 cases. Note that while MICRE covers a much longer period than MARCUS and CAPRICORN, the two radiosonde launches per day (as compared to four or more on the ships) reduces the overall number of cases at Macquarie Island. We tested the impact of differing seasons and SST on cloud boundary distributions, but neither was found to significantly affect the distributions or bias our results. Therefore, we use all three campaigns together to ensure a large enough sample size of 379 data points. In contrast, we have a total of 1,642 data points available for the ENA site.

2.3. Large-Scale Measures of Boundary Layer Stability

In this analysis, we focus on three separate large-scale measures of boundary layer stability, that have been shown to correlate well with low-level cloud spatial extent and morphology:

1. *The LTS* (Klein & Hartmann, 1993): the difference in potential temperature between 700 hPa and the surface air, obtained here with radiosoundings and surface meteorology observations ($LTS = \theta_{700hPa} - \theta_{surf}$).
2. *The EIS* (Wood & Bretherton, 2006): a correction of LTS that takes into account the impact of a moist adiabat lapse rate above the LCL. The additional information is obtained with the radiosoundings of temperature and geopotential heights, as well as surface meteorology data: $EIS{=}LTS - \Gamma_m^{850}(Z_{700} - LCL)$ where LCL is the lifting condensation level, Z_{700} the altitude of 700-hPa level and Γ_m^{850} is the moist lapse rate at 850 hPa. To obtain LCL, we use the Epsy approximation $\mathrm{LCL} = 125\,(T - T_\mathrm{d})$ where T_d is the dew point temperature obtained using the meteorological station temperature and a fixed relative humidity of 80% as in Wood and Bretherton (2006). The lapse rate is obtained using the formula given in Wood and Bretherton (2006) using both near-surface meteorological station temperature and the radiosonde 700-hPa temperature.
3. *The MCAO M index* (Fletcher et al., 2016a): the difference in potential temperature between the skin and the 800-hPa level, obtained with MERRA-2 and the radiosoundings ($M = \theta_{skin} - \theta_{800}$). We stress here that M is based on the surface "skin" temperature and not the "near-surface air" temperature.

These measures were found to be highly correlated with CF, or cloud morphology, but there is some evidence that these same measures correlate well with cloud base or top heights, that is, the cloud vertical distribution. Kawai et al. (2015) found that LTS and EIS were well correlated with CTHs at multiple latitudes, while Naud et al. (2018) found similar results for the ENA site, but better correlations with M. So next we explore whether these metrics relate to cloud boundaries in the SOs.

3. Relationships Between Cloud Boundaries and Stability Measures in the SO

For all the analyses, as mentioned above, we only impose that MERRA-2 vertical velocity indicates subsidence and the radar observations report clouds with tops below 3 km. This is what was imposed in Naud et al. (2018). However, the SO region exhibits different conditions from what is typically found at the ENA, so we first examine the large-scale context for the observations we selected and compare the two locations.

3.1. Comparison of the Large-Scale Conditions in SO With Those at ENA

The ENA site experiences relatively mild SST year round. When subsidence occurs and clouds below 3 km are present, the mean SST is 293 ± 3 K (mean ± one standard deviation), with a difference between the maximum and minimum of ~12 K. The SO is much colder, with a mean SST of 278 ± 3 K for our samples, and shows larger variability than ENA: The difference between maximum and minimum is ~20 K because of the wide range of latitudes that are sampled. Similarly, near-surface air temperatures are slightly less variable at the ENA site with a spread of ~17 K, and mean of 292 ± 4 K, whereas our SO samples display a spread in near-surface temperatures of ~20 K and a mean of 278 ± 4 K. We also note that the near-surface air temperature at the ENA displays slightly more variability than the SST, while the SO data sets show similar variability despite the wider range of latitudes and temperatures covered.

To further characterize the differences in the large-scale context (again for cases of subsidence and low-level clouds), we also composite MERRA-2 SLP fields. For the ENA site, we use a ±10° longitude-latitude region centered on the Graciosa Island. For the SO we use the SLP fields for a region of the same size centered on the Macquarie Island and the ship locations. The composites show clear differences in the distribution of SLP for the SO (Figure 2a) and ENA (Figure 2b) data sets for our specified conditions (i.e., when subsidence and low clouds are coincident with the sounding). At the ENA site, which is situated very close to the climatological feature known as the Azores high, SLPs are much larger than for the SO data set: It shows a clear anticyclonic area with SLPs greater than 1,023 hPa (Figure 2b), while SLPs do not exceed 1,009 hPa in the SO composite (Figure 2a). For the SO data sets, the SLP field shows a very zonal pattern with an average of 997 hPa. These results suggest significant differences in the synoptic conditions when low clouds are present at the ENA site and the SO locations.

On the other hand, composites of the SLP anomaly (compared to a 4-year yearly average for ENA—using 2015–2018—and a 2-year average for the SO locations—using 2016–2017) reveal that the anomalous circulation at the two locations is qualitatively rather similar: subsidence with low clouds occur during the transition period between an existing anomalously low pressure system to the east and the arrival of anomalous anticyclonic circulation to the west (Figures 2c and 2d). This said, the absolute values of the anomalies are weaker in the SO than in the ENA area. The absolute SLP and anomaly composites suggest that the anticyclones that affect the SO region are much weaker than those that are present at ENA. One consequence of the much more zonal SLP pattern in the SO is that the winds are much stronger than at the ENA site (Figure S2). Therefore, while the anomalies are consistent, the differences in absolute value of SLP and wind profiles indicate that the boundary layer structure at the ENA would be that of more quiescent (and warmer) conditions as compared to the SO region sampled here. Taking into account these regional differences, we next test whether, nevertheless, cloud boundaries in the SO region sampled here relate to the three measures of stability introduced in section 2.3 as was found for the ENA data set (Naud et al., 2018).

3.2. The Relationship Between Cloud Boundaries and Large-Scale Boundary Layer Stability Measures in the SO

Using all hourly data from all three campaigns, we calculate the linear Pearson correlation coefficient between cloud base heights (CBHs), CTHs, and CTT and the three measures of stability (Table 1). These correlation coefficients are calculated for all three campaigns data combined as well as separately for each campaign. For all three cloud parameters, the highest correlation coefficient always occurs when using M as the stability measure (Figure 3 and Table 1): 0.51 for CBH, 0.42 for CTH, and −0.79 for CTT for all three campaigns together. The larger correlation coefficient for CTT than CTH probably stems from the large correlation between the temperature at 800 hPa and CTT.

The strong correlations between cloud boundary parameters and M are also true for MICRE and MARCUS data sets individually but not for CAPRICORN. The CAPRICORN data set gives slightly larger (in absolute

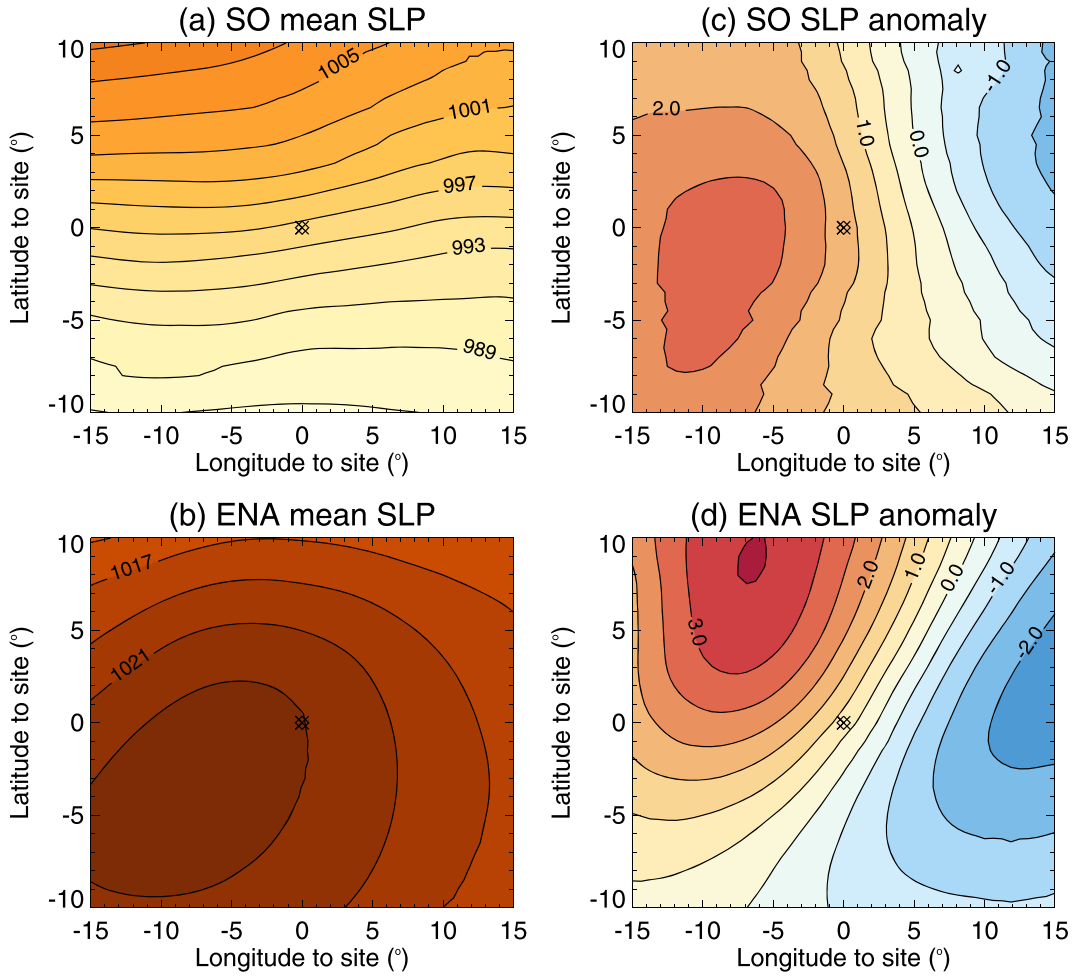

Figure 2. Composites of MERRA-2 sea level pressure when conditions of subsidence with measurements of low-level clouds are collected for (a) the Southern Ocean campaigns and (b) the ENA site and anomaly compared to a yearly mean SLP composite for (c) Southern Ocean and (d) ENA. The anchor of the composites, indicated with a cross (x) in a black box, matches the location of the Macquarie Island and ships for the Southern Ocean (a, c) and the ENA site (b, d).

value) coefficients for CTH and temperature when using LTS as the stability measure rather than M ($R = -0.36/0.66$ for LTS vs. $0.32/-0.64$ for M; Table 1). Not surprisingly, the Spearman's rank correlation coefficient and significance test indicate that the smaller CAPRICORN data set has overall lower confidence levels. We indicate in Table 1 where the confidence levels are less than 95% or between 95%

Table 1
Linear Pearson Correlation Coefficients Between CBH, CTH, CTT, and LTS, EIS, M for the Entire Southern Ocean Data Set and for Individual Campaigns (MICRE, MARCUS, CAPRICORN-1 and CAPRICORN-2)

	Stability measure		
Cloud boundary measure	LTS	EIS	M
CBH	−0.40 (−0.49, −0.41, −0.13*)	−0.38 (−0.47, −0.42, −0.05*)	0.51 (0.64, 0.50, 0.21**)
CTH	−0.35 (−0.40, −0.28**, −0.36**)	−0.33 (−0.35, −0.29**, −0.32**)	0.42 (0.50, 0.36, 0.32**)
CTT	0.65 (0.63, 0.68, 0.66)	0.47 (0.53, 0.46, 0.38**)	−0.79 (−0.86, −0.76, −0.64)

Note. A Spearman's rank correlation significance test indicates all correlations are significant to better than 99.99% confidence
*Confidence levels <95%. **Confidence levels between 95% and 99.99%.

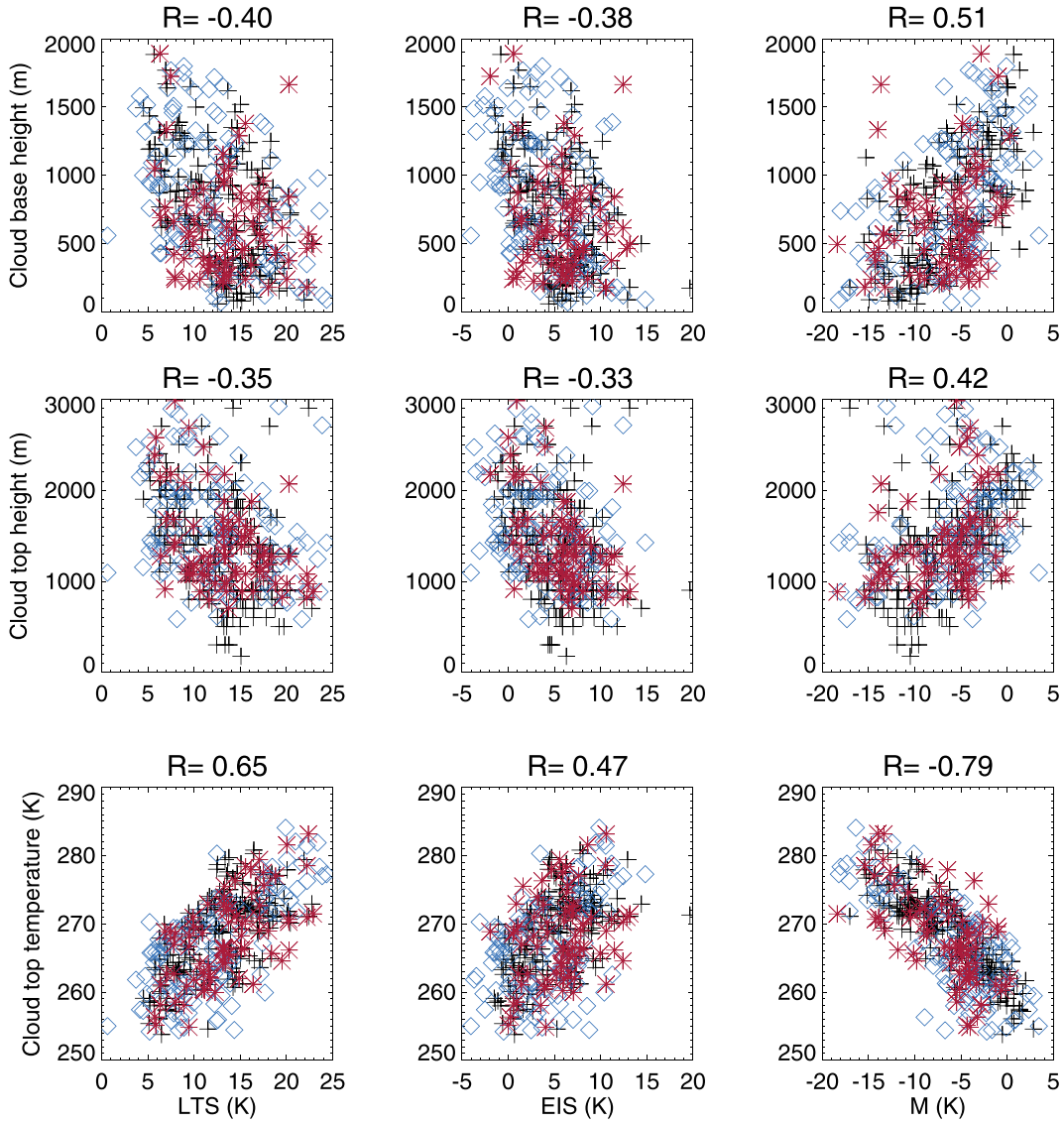

Figure 3. Relationship between (from top to bottom) cloud base height, cloud top height, cloud top temperature and (from left to right) lower tropospheric stability (LTS), estimated inversion strength (EIS), marine cold air outbreak index M, for the MICRE (black), MARCUS (blue), and CAPRICORN-1 and CAPRICORN-2 (red) campaigns. The linear Pearson correlation coefficient is indicated at the top of each panel and is calculated for all three campaigns combined.

and 99.99%. In particular, the weak correlations of CBH with the CAPRICORN data set are not significant at the 95% level of confidence and the contradictory results here are likely due to the smaller range of variations encountered in this data set.

The stronger correlations with cloud boundaries found for M than LTS or EIS for the SO data sets are consistent with those for the ENA site (Naud et al., 2018), despite the differences in the large-scale atmosphere and ocean conditions discussed above. While these SO campaigns and the ENA data sets sample only two specific regions and therefore are not a global sample, the strength of M as a predictor of cloud boundaries appears to hold.

As observed in the subtropics in Bretherton et al. (2010) during VOCALS-Rex, a decrease in stability is accompanied by a deepening of the boundary layer and a transition from well mixed to decoupled boundary layers. Conjunctly, in their observations, one can clearly see that the CTHs increase and so do the CBHs. The good correlations we find here suggest that as instability and boundary layer depth increase, CBHs elevate (at least on average) in the midlatitudes as well.

Another point regarding the role of stability for CF and morphology was raised by Myers and Norris (2013): Subsidence strength also impacts CF, and they found covariability of CF with both EIS and subsidence. We explored this covariability for our data sets. For weak subsidence, we found some conjunct relationship of CTH with both EIS and subsidence strength; however, this relationship is less clear for larger values of subsidence strength (above ~6 hPa hr^{-1}), which are more frequent in the extratropics. Also, no clear conjunct relationship was found when using M (see Figure S3–S5 and discussion in the supporting information).

While there is an extensive literature on how LTS or EIS relate to the boundary layer structure and to the cloud organization and morphology, there is much less information on the relationships with the M index. Fletcher et al. (2016b) examined in detail cloud properties when the M index is positive (i.e., in conditions of cold air outbreak), but not when it is negative. McCoy et al. (2017) investigated the relationship between the M index and the spatial organization of stratocumulus fields but did not investigate the vertical structure of the boundary layer. So next we explore how the boundary layer structure changes as M changes to (1) verify that this is consistent with what has been found for other stability measures and (2) whether the two locations show similar structures.

3.3. Boundary Layer Structure as a Function of M for the SO and ENA Site

For this analysis, we use radiosoundings to study changes in temperature and dew point profiles as a function of M. Previous studies show that as LTS increases, stability increases, boundary layers thin (inversion top gets closer to the surface), and clouds transition from cumulus to stratocumulus fields. We expect a similar behavior with M: As M increases (becomes less negative), stability decreases and clouds transition from stratocumulus to cumulus fields. This should be accompanied by an increase in boundary layer depth and a weakening of the inversion as the stability decreases.

We partition the ENA and SO data sets into five subsets based on the value of M: (a) $M < -12.5$, (b) $-12.5 < M < -10$ K, (c) $-10 < M < -7.5$ K, (d) $-7.5 < M < -5$ K, and (e) $M > -5$ K. While these categories distribute the ENA profiles relatively evenly, with between 13% and 26% of profiles per category, for the SO data sets we find a much larger fraction of the profiles in the large M category, which includes cases of cold air outbreak (44% for $M > -5$ K vs. between 13% and 17% for all other categories). This suggests more frequent unstable cases in the SO than ENA cases. The mean (which we also call the composite) profile in each category is obtained by using the CTH for each profile as the anchor of all profiles before the average is calculated. In other words, the profiles are averaged such that the base of the inversion coincides across all profiles. To do this, we use the same method as Norris (1998): For each profile in a given M category, the geopotential height profile is normalized by the corresponding CTH, and projected into a common grid, before the average of dry and dew point temperatures is performed. Then the vertical axis of the composite profiles is rescaled to the mean CTH (obtained for all cases per M category). This way, the vertical axis of the composites remains referenced to mean sea level.

Starting with the ENA profiles (Figure 4, top row), as M increases from stable to unstable cases, the depth of the boundary layer increases while the mean profiles of temperature and dew point show a fairly well mixed boundary layer below the inversion. The inversion is somewhat sharper for the most stable cases, consistent with previous work in the subtropics (e.g., Albrecht et al., 1995). In the last category ($M > -5$ K) the boundary layer is somewhat drier (the dew point and dry air temperature profiles show a clear separation), consistent with the transition between stratocumulus and trade inversion cumulus conditions in the subtropics (e.g., Wood, 2012, and reference therein). For the SO profiles (Figure 4, lower row), the inversion is weaker than at the ENA site but again appears strongest for the lowest M bin. While drying for the largest M bin is also apparent, the boundary layer is not nearly as deep.

To try and better visualize differences in mixing below clouds, we also average the potential temperature profiles at both locations using the same method as above (Figure 5). While individual profiles often show a weak inversion and wind shear associated with a secondary inversion (which may be a common feature of SO boundary layer structure; Hande et al., 2012), the averaging tends to blur any signature of potential decoupling. This said, the mean ENA potential temperature profiles resemble the idealized profile used by Wood and Bretherton (2006) to derive their estimate of inversion strength (EIS): They assume a well-mixed layer from surface to LCL (a constant potential temperature), a moist adiabatic lapse rate in the decoupled layer that contains the cloud and a marked inversion. The mean SO potential temperature

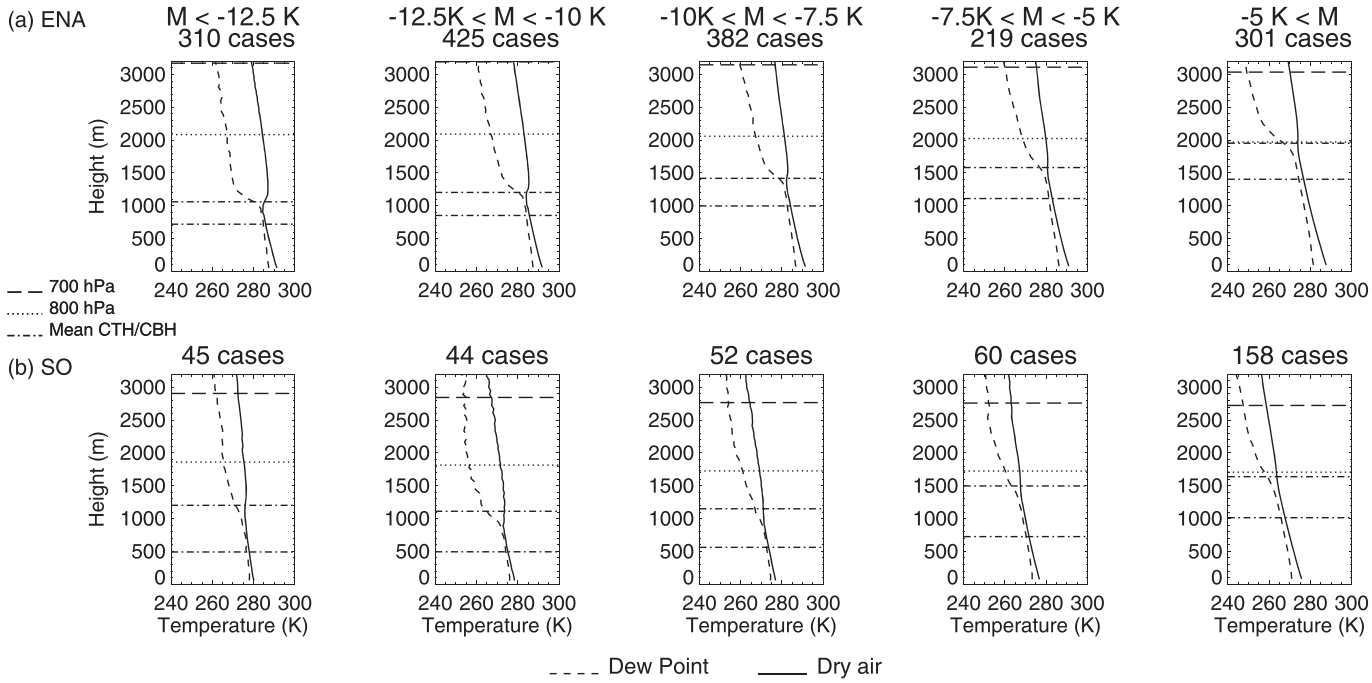

Figure 4. Mean dry air temperature (solid) and dew point temperature (dashed) profiles averaged in five M index bins, of increasing value from left to right: M < −12.5 K, −12.5 < M < −10 K, −10 < M < −7.5 K, −7.5 < M < −5 K, and −5 K < M. The profiles are obtained at the (a) ENA site and (b) during the Southern Ocean campaigns. The horizontal dash-dotted lines show the mean CTH and (below) CBH per bin, the dotted line the mean 800-hPa level, and the wide dashed lines the 700-hPa level. The number of cases that fall into each M category is indicated at the top of each panel.

profiles do not display a region with constant potential temperature near the surface but instead a steady increase from the surface to the inversion for all M categories. The M > −5-K category might be an exception, as the profiles of potential temperature for this category are more upright up to 500 m. The subcloud layer is, however, more well mixed than Figure 4 suggests, because it displays a nearly constant (on average) virtual potential temperature (Figure S6). This might be caused by larger relative humidity near the surface in the SO compared to the ENA (as suggested in Figure 4), which also affects stability. Virtual potential temperature composite profiles, averaged using cloud base rather than top heights (Figure S6) did not, however, provide any clearer transition from well mixed to decoupled boundary

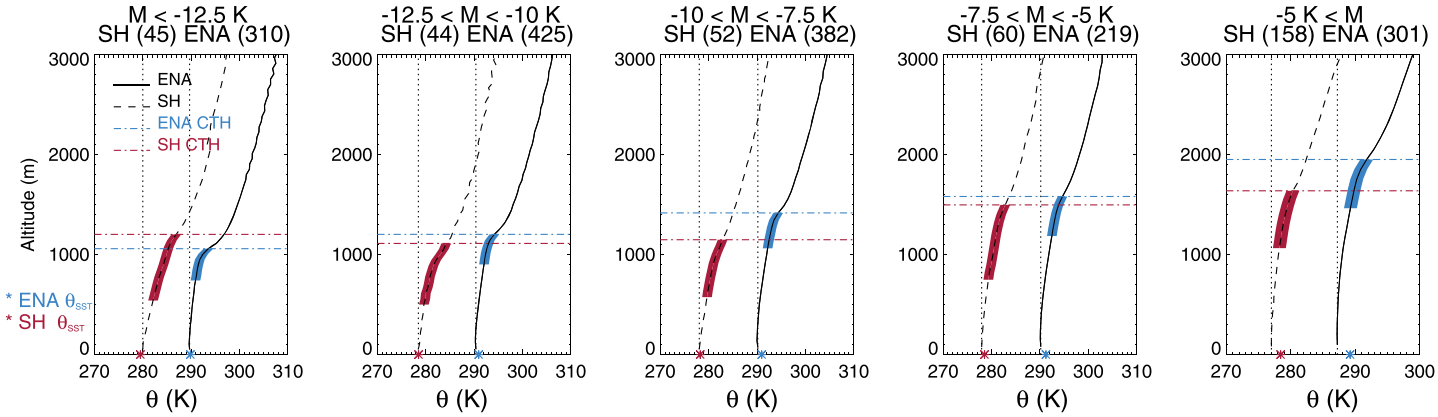

Figure 5. Mean profiles of potential temperature for five distinct M categories using the ENA data set (solid) and the SO data sets (dashed). The vertical dotted lines indicate the potential temperature at the lowest profile level. The horizontal dot-dash lines show the location of the mean cloud top height for ENA (blue) and SO (red). The thicker colored portions of the profiles identify the region between mean cloud base and mean cloud top heights. The skin potential temperature is indicated with the star symbols, in red for SO, and blue for ENA. The number of profiles that fall in each M category is given in parenthesis for each location.

layers in the SO (as has been observed in the subtropical regions, e.g., Ghate et al., 2015). Figure 5 also reveals a tendency for the clouds to be much deeper (physically thicker) for the SO than ENA data sets. At both locations, when comparing the skin potential temperature (denoted with a star) to the potential temperature near the surface, there is a clear progression of the air with respect to skin temperature: with similar mean air and surface temperature for the lowest M category to increasingly lower air than surface temperature for cold air outbreak conditions at larger M categories.

In summary, while there is a similar evolution of the ENA and SO boundary layer structure with reduced stability and higher inversion levels as M increases, there are clear differences between the two locations: (1) Inversions are much stronger (sharper) at the ENA, and (2) the planetary boundary layer (PBL) is deeper for a given range of M; (3) the SO data deviate from the idealized thermodynamic vertical structure proposed by Wood and Bretherton (2006). While providing important information on the different environments at the ENA site and SOs when low-level clouds occur, the composite profiles do not provide a clear indication as to why M would relate better to cloud boundaries than LTS or EIS. So next we examine LTS, EIS and M in more details for their relationship with cloud boundaries.

4. Why Does M Correlate Better With Cloud Vertical Structure Than LTS or EIS?

When examining the relationship between cloud boundaries and the three measures of LTS, EIS, and M, Table 1 and Figure 3 revealed that base and top heights (1) correlate better with LTS than EIS and (2) correlate better with M than LTS. So now we examine these two results in more details to try and explain the better performance of M as a predictor of cloud boundary heights.

4.1. Examining the Better Correlations With LTS Than EIS for Cloud Boundaries: The Role of the Inversion Strength

As illustrated in Table 1 and Figure 3 for the SO data sets, we find better correlation coefficients when using LTS than EIS for all three cloud boundary measures. To try and understand why this is, we use the radiosonde profiles to obtain the actual inversion strength, which both LTS and EIS are designed to approximate. The inversion strength per sounding is the difference in potential temperature between top and base of the inversion ($\Delta\theta$; Wood & Bretherton, 2006, their equation 1 relates this quantity to the characteristics of an idealized potential temperature profile). For this we isolate the level of maximum increase in temperature between 500 and 3,000 m to locate the inversion and define base and top of the inversion layer as the levels at which the temperature change becomes positive for base and negative again for top (similar to the method described in Rémillard et al., 2012). We then examine the Spearman's rank correlation coefficients between EIS and $\Delta\theta$, and between LTS and $\Delta\theta$. We perform these calculations for both the ENA and SO data sets. The Spearman's rank coefficient for EIS versus inversion strength is 0.51 for the ENA and 0.44 for the SO data sets and for LTS it is 0.50 for the ENA and 0.41 for the SO data sets. We note that when we average our data sets into monthly means before we calculate EIS and LTS, these same coefficients increase in magnitude. This is because EIS and LTS were designed for monthly data sets, not hourly instantaneous data as in this study. Nevertheless, these results confirm that EIS is by design better correlated with inversion strength.

However, when we tested the degree of correlation between CBH and inversion strength, we found it to be small for both locations: $R = 0.11$, and similarly for CTH (0.02 for SO, −0.05 for ENA) and temperature ($R = 0.00$ for SOs and 0.15 for ENA). So while inversion strength correlates well with CF, it does not correlate with cloud boundary locations. Presumably, cloud boundaries are not driven by inversion strength but instead more so by vertical stability below the inversion. Therefore, the correction that uses the moist adiabat and LCL in the EIS definition is not helping better predict cloud boundaries, and LTS alone gives better results. Alternatively, the better performance of LTS might be because it simply estimates the mean lapse rate of the lower atmospheric column, and as such is a better approximation of its stability. Given that their definitions are rather similar and that they are fairly well correlated to one another, we next explore in more details both LTS and M for their relationship with cloud boundaries.

4.2. Examining the Better Correlations With M than LTS for Cloud Boundaries: The Impact of Surface and Upper-Level Potential Temperature

While M correlates better with cloud boundaries than LTS, it is unclear whether this is because (1) the upper-level temperature variable is simply closer to the true cloud top (i.e., 800 hPa vs. 700 hPa,

Table 2
Linear Pearson Correlation Coefficients Between CBH, CTH, CTT, and the Difference in Potential Temperature Between 700 hPa and the Near Surface (700 − Surf; = LTS), 800 hPa and Near Surface (800 − Surf), 700 hPa and Surface (700 − Skin), and 800 hPa and Surface (800 − Skin; = −M); and Absolute Difference in Coefficients When Changing From 700 to 800 hPa for a Given Surface Temperature (Change 700 to 800) and When Changing From Near-Surface to Skin Temperature for a Given Upper Level (Change Surf to Skin)

Location	Cloud boundary	700 − surf	800 − surf	700 − skin	800 − skin	Change 700 to 800	Change surf to skin
ENA	CBH	−0.27	−0.41	−0.34	−0.46	0.14/0.12	0.07/0.05
	CTH	−0.34	−0.47	−0.43	−0.53	0.13/0.10	0.09/0.06
	CTT	0.43	0.56	0.58	0.67	0.13/0.09	0.15/0.11
SO	CBH	−0.40	−0.53	−0.42	−0.52	0.13/0.10	0.01/0.02
	CTH	−0.35	−0.43	−0.36	−0.42	0.08/0.06	0.01/0.01
	CTT	0.65	0.74	0.72	0.78	0.09/0.06	0.07/0.04

respectively) and is therefore simply more closely correlated to the true temperature inversion magnitude or (2) the use of "skin" rather than "near-surface" temperature effectively includes some information on the surface forcing, that is, information on whether the surface layer—air closest to the surface—is stable (with respect to the air immediately above it) or not. Thus, M potentially includes some information on the surface sensible heat flux (based on the bulk formula used for surface fluxes). Therefore, we examine the linear Pearson correlation coefficients between the three cloud parameters and different combinations of potential temperature contrasts (Table 2): 700 hPa minus surface air (hereafter referred to as 700 − surf; i.e., LTS), 800 hPa minus surface air (referred to as: 800 − surf), 700 hPa minus skin (referred to as: 700 − skin), and 800 hPa minus skin (referred to as: 800 − skin; i.e., −M). To ensure that the correlation coefficients are robust, we also verify that a Spearman's rank correlation provides similar results and find that in all cases the correlation coefficients are significant at a confidence level above 99.99%.

Starting with ENA, we find that regardless of which surface temperature is used, using the 800-hPa level systematically gives higher correlation coefficients than the 700-hPa level with an absolute change of about 0.1 in the linear Pearson correlation coefficient (Table 2) with all three cloud boundary parameters. Similarly, regardless of the upper-level choice, using the skin temperature gives better correlations than surface air with a change in correlation coefficient between 0.05 and 0.15. For the ENA data, while both the near-surface temperature choice and the upper-level temperature choice impact the correlations when using M versus LTS, it appears that including the effect of skin temperature is slightly less important than using 800 hPa.

For the SO data set the improvements in the linear correlation coefficients are more subtle when using 800 instead of 700 hPa for CTH/temperature (change of 0.06 to 0.09) but consistent with the ENA data set for CBH. They are, however, virtually null when using skin instead of near-surface temperature for all three cloud boundary measures (change of −0.02 to 0.07). In other words, changes in the correlation coefficients when using M in place of LTS seem dominated by changes in the upper-level height for the SO data sets.

There are differences between the two locations: (1) The correlation coefficients are larger when using LTS for the SO than ENA data sets and (2) the impact of using skin rather than air temperature is larger for ENA than the SO. The near-surface and skin temperatures are well correlated at both locations: The linear Pearson correlation coefficient between near-surface and skin temperatures is about 0.90. We saw earlier (cf. section 3.1) that there is a slightly larger variability in air temperature than skin temperature at the ENA, which could be caused by the impact of surface heating during daytime at this land-based location. However, when we redid the calculations of Table 2 separately for daytime and nighttime observations at the ENA, the results did not change. The site is situated along the northern coast of the Graciosa Island, which displays some variations in topography with elevations up to 400 m south of the site (e.g., Giangrande et al., 2019). When we removed southerly wind conditions from the ENA data set, the sensitivities of Table 2 did change slightly, enough to suggest that the island has some impact on the observations but not enough to bring sensitivities to surface temperature on par with what is found with the SO data sets.

While it appears that the better correlation between cloud base and top heights and the M index has more to do with using 800 hPa, a level closer to cloud top, skin temperature is in fact as important for both locations

when examining CTT. To summarize, using an upper level closer to cloud top and taking into account the impact of the surface forcing both explain the better correlation with cloud boundaries obtained with M compared with LTS, but the use of skin instead of near-surface temperature helps more specifically for CTT.

5. Applicability to Model Evaluation

The correlations reported in sections 3 and 4 are potentially useful for the development and evaluation of parameterizations for climate models in at least two ways: (1) The relationship between cloud properties and M could be incorporated into cloud parameterizations (e.g., the Geophysical Fluid Dynamics Laboratory [GFDL] climate model uses EIS in its convection scheme; Zhao et al., 2018) and (2) the correlations from observations can serve as benchmarks for evaluating the models.

To provide a benchmark, in Figure 6 we examine the joint distributions of M with CBH, top height and top temperature from observations. Overlain are linear regressions (see also Table 3). The regressions present some differences between the two locations: For both cloud base and top heights the rate of change in height for a given change in M is slightly steeper at the ENA than for the SO, more so at cloud top (72.60 $\pm$ 2.88 vs. 48.96 $\pm$ 5.62 m K^{-1}) than base (55.94 $\pm$ 2.68 vs. 51.33 $\pm$ 4.54 m K^{-1}; Table 3 and Figures 6a, 6b, 6d, and 6e). However, for CTTs, the rates of change at both locations are very close (-0.97 ± 0.03 vs. -1.05 ± 0.05 K K^{-1}), but clouds tend to have cooler tops (~10-K difference) in SO than at ENA (Table 3). To minimize the impact of the climatological temperature differences, we performed another regression using CTT minus SST (i.e., CTT-SST) instead: This gives very similar relationships between CTT-SST and M at both locations (last row of Table 3). Despite some obvious caveats, these relationships could be used in a similar fashion as what was implemented in different models using LTS and EIS: Köhler et al. (2011) included a test in their boundary layer parameterization to help the transition between stratocumulus and cumulus clouds using a threshold imposed on LTS, while Zhao et al. (2018) implemented a similar test using EIS instead. The caveats are that (1) the results presented here are obtained with time series of point measurements, whereas current GCMs are typically providing cloud and meteorological parameters at approximately 100-km by 100-km horizontal resolution; (2) we only test two specific locations over a limited period of time.

Here we examine output from the National Center for Atmospheric Research (NCAR) Community Atmospheric Model version 6 (CAM6; see Gettelman et al., 2018, for a description of the model's physics) to determine if it produces a similar relationship for cloud boundaries. For CAM6 we obtained temperature, geopotential height, pressure and CF profiles, 500-hPa vertical velocity, and surface pressure and temperature. We use the surface properties and temperature profiles to estimate M for the grid cell containing the ENA site and for a region from 66°S to 40°S between 80°E and 160°E. The output is available on 6-hourly time steps and in a 1.25° $\times$ 0.943° longitude-latitude grid on model levels, for a 5-year period (forced with SST from 2010 to 2014).

Because we do not have cloud base and top heights as model output, we use the CF profiles instead. The observations have a finite sensitivity to hydrometeors, but the model does not suffer from this issue and can thus produce CFs much smaller than any instrument can detect. Therefore, to obtain cloud base and top height in a manner that is, to some extent, consistent with what is observed, we impose a threshold on the CF at each level in the model columns. Note that the observations do not provide information on cloud liquid water content or other cloud properties. Because the radar lidar-based observations are available at most every 4 s and we use hourly periods, cloud boundary observations are reported for CFs greater than 10^{-3} at each atmospheric level. We use the same threshold for the modeled CF. Then for each model column cloud base is the first level above the surface with CF > 10^{-3} and cloud top the last level above that base with CF > 10^{-3}. As with the observations, we extract CTT based on this CTH from the temperature profiles. Then we select the cases for which CTH < 3 km and modeled 500-hPa vertical velocity indicates subsidence. We acknowledge that this method has its limitations as we describe below, in particular for diagnosing CBH.

For the ENA grid cell and for all grid cells in the SO region, using all seasons over the 5 years, we examine the relationship between CBH, CTH and CTT, and M (Figure 7). Note that because the modeled cloud profiles are provided on model levels (and not interpolated to a much finer grid), there are visible gaps in the distributions as levels separation increases aloft. We also perform linear regressions for each pair, as listed in

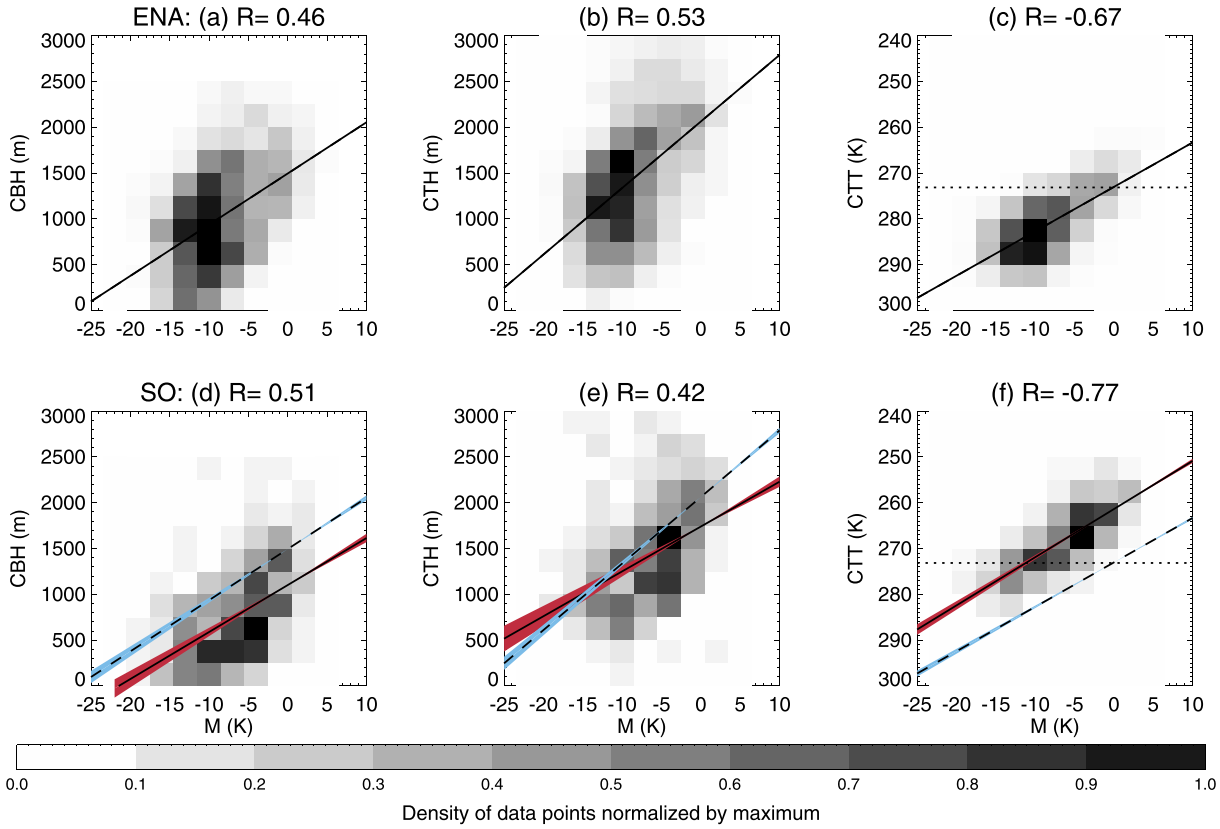

Figure 6. Density of data points (normalized by maximum) for subsidence conditions and clouds below 3 km, as a function of cloud base height (a, d), cloud top height (b, e), cloud top temperature (c, f) and M for the ENA (a–c), and the Southern Ocean (d–f) data sets with linear regression lines in solid black for each pair, and regression lines from the ENA as dashed lines. The regression parameters are given in Table 3. The dotted lines in (c) and (f) indicate the 273.15-K level. The linear Pearson correlation coefficient for each pair is provided at the top of each panel. The blue and red highlights indicate a ±1 sigma of the regression for ENA and SO data sets, respectively.

Table 3. For cloud-top temperature and height we find that CAM6 has a relationship with M that is close to the observations for both ENA and the SO. However, the model predicts a slightly steeper slope than observed (e.g., 84.71 ± 1.41 for the model versus 72.60 ± 2.88 m K^{-1} for observations of CTHs at ENA). This is found regardless of whether we use a threshold on the CFs or not. In other words, for a given M, the model tends to predict clouds that are slightly too high and too cold at the top. This is still true when the CTT is scaled with SST, that is, when the impact of an error in SST is partially removed (last row of Table 3). More significant disagreements are found for CBHs: For a given M, the model predicts a CBH much lower than observed (Figure 7 and Table 3). Nevertheless, the model reports a realistic correlation between CBH and M at the ENA site, albeit with a much weaker correlation for the SO cases. However,

Table 3
Slope (m K^{-1}), Intersect (m), and Standard Error (in Parenthesis) From a Linear Regression of Cloud Boundary Measures (CBH, CTH, CTT, and Difference Between Cloud Top Temperature and Sea Surface Temperature—CTT-SST) Versus M Parameter for Observations and CAM6 Output at the ENA Site and in the Southern Ocean (SO) Region

	Observations		CAM6	
	ENA	SO	ENA	SO
CBH	55.94 M + 1,495 (2.68)	51.33 M + 1,102 (4.54)	29.12 M + 830 (0.85)	13.44 M + 579 (0.03)
CTH	72.60 M + 2062 (2.88)	48.96 M + 1,740 (5.62)	84.71 M + 2,207 (1.41)	54.09 M + 1960 (0.05)
CTT	−0.97 M + 273 (0.03)	−1.05 M + 261 (0.05)	−1.16 M + 269 (0.01)	−1.31 M + 258 (0.00)
CTT-SST	−0.85 M − 18 (0.02)	−0.95 M − 16 (0.03)	−0.98 M − 21 (0.01)	−0.96 M − 20 (0.00)

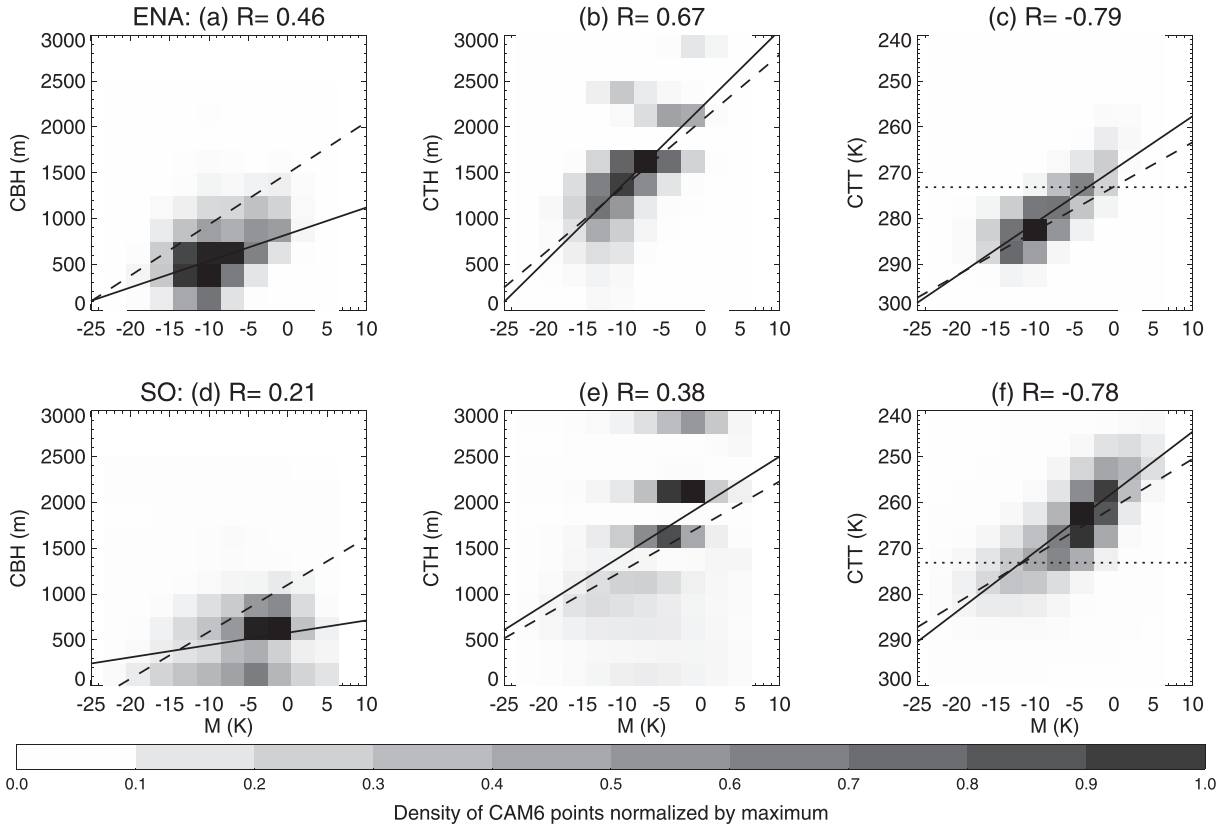

Figure 7. Density of CAM6 grid cells (normalized to maximum) for subsidence conditions and clouds below 3 km, as a function of cloud base height (a, d), cloud top height (b, e), cloud top temperature (c, f) and M for the ENA (a–c), and in the Southern Ocean (d-f) with linear regression lines in solid black for each pair, and regression lines from the corresponding observations (cf. Figure 6) as dashed lines. All regression parameters are provided in Table 3. The dotted lines in (c) and (f) indicate the 273.15-K level.

we note that changing the CF threshold to obtain CBH has a significant impact on the results given here (not shown). Therefore, we cannot evaluate the relationship between cloud base and M with confidence with this threshold approach. Thus, while the sensitivities at cloud top appear robust (and suggest that the model tends to place low-level cloud tops at cooler temperatures than observed for a given M range), it appears that a modification to the CAM6 output to provide a cloud base comparable to the observations will be needed to more fully evaluate the model. We add that this applies to any model to be evaluated in this way.

6. Conclusions

Using ground- and ship-based observations in the SO, along with data from the ENA site, we examine the relationship between boundary layer cloud boundaries (CBH, CTH, and CTT) and different measures of LTS in conditions of subsidence. Despite differing large-scale conditions at the two locations, with much lower SLPs and colder temperatures in the SO, at both locations the strongest correlation is found with the MCAO parameter M for cloud base, top height, and top temperature rather than LTS or EIS. It appears that this might be in part because the inversion strength, which LTS and EIS are designed to estimate, does not correlate with cloud top or base heights. In turn, this might explain why EIS gives lower correlation coefficients with cloud boundaries than LTS (also noted for CTHs by Kawai et al., 2015). This and the similarity between LTS and M definitions motivated further examination as to why M correlates better than LTS with these cloud properties. They differ in that (1) M uses an upper surface of 800 hPa, which is typically closer to cloud top than the 700 hPa used in LTS and (2) M uses skin temperature, while LTS uses surface air temperature. We find that 800 hPa provides a better correlation than 700 hPa regardless of the surface parameter used for all three cloud boundary measures and two locations examined here. Using the skin temperature gives better correlation than surface air regardless of the choice of upper level mainly for CTT at both

locations, or all three parameters for ENA only. At the ENA, using skin rather than air temperature has a much larger positive impact on the correlations than for the SO data sets. This might be because near-surface air temperatures display greater variability at the ENA than in the SO, and greater than SST variability itself.

Much stronger inversions at the ENA might explain why the slope of the regression is stronger for this data set than SO cases when considering cloud base and top heights versus M. However, the slope is consistent in both regions for CTT, with colder cloud tops in the SO than ENA for a given M. While these disparities between the two locations complicate a straightforward application of the regression to help improve model parameterizations, it could be generalized by introducing other simple measures, for example, scaling cloud boundaries using SSTs.

Overall, the CAM6 GCM reproduces the relationship between CTH and temperature and M at both ENA and SO. The model has more difficulty representing the relationship between CBH and M, though our diagnostic of cloud base is not robust enough to ascertain (see section 5). While the method used here to extract cloud base information limits confidence in our conclusions regarding CBHs in CAM6, the model clearly tends to predict a cloud top that is colder than observed for a given M. While this is a succinct evaluation, it might help narrow down the conditions in which parameterizations might need improvements. A similar test might also help monitor future versions of the model, and might help test the impact of higher vertical resolution.

This study is conducted in two very specific regions, and the next step will be to use satellite-based observations to test whether, at least at cloud top, similar relationships are verified over global oceans. Of importance as well for model evaluation, the impact of coarser spatial and temporal resolutions on the relationships explored here will need to be evaluated. Finally, previous work suggests that the M parameter might be a good predictor of cloud properties in the midlatitudes but not in the subtropical regions (McCoy et al., 2017). This might also be a useful test to be applied to GCMs. The fact that it might not be as good a predictor in the subtropics highlights the importance of the surface forcing and advection in the extratropics for clouds. This might have implications for predicting cloud changes in a changing climate: feedbacks that are predicted for the subtropics might be different in the midlatitudes where the atmospheric large-scale circulation has a much more prominent impact on boundary layer clouds.

Data Availability Statement

The MERRA-2 files were obtained from the NASA Goddard Earth Sciences Data and Information Services Center https://disc.sci.gsfc.nasa.gov/ (doi: 10.5067/AP1B0BA5PD2K). All ARM observations were obtained from the website (https://www.archive.arm.gov/discovery/), the sounding profiles (https://doi.org/10.5439/1021460), the meteorological station data (https://doi.org/10.5439/1025220), and the cloud radar-lidar combined vertical profiles (https://doi.org/10.5439/1350630 and https://doi.org/10.5439/1350613). The BoM data sets are available on the CSIRO Data Access Portal (https://www.marlin.csiro.au/geonetwork/srv/eng/search#!c88d62e1-43a2-4790-9fe6-5e4be21023b9).

Acknowledgments
The work is funded by the U.S. Department of Energy Office of Science Grants DE-SC0016344 and DE-SC0018626 as part of the Atmospheric Systems Research program. We thank Hideaki Kawai and two anonymous reviewers for their insightful comments that have help significantly improve this analysis.

References

Ahlgrimm, M., & Forbes, R. (2014). Improving the representation of low clouds and drizzle in the ECMWF model based on ARM observations from the Azores. *Monthly Weather Review*, *142*(2), 668–685. https://doi.org/10.1175/MWR-D-13-00153.1

Albrecht, B. A., Jensen, M. P., & Syrett, W. J. (1995). Marine boundary layer structure and fractional cloudiness. *Journal of Geophysical Research*, *100*(7), 14,209–14,222.

Atmospheric Radiation Measurement (ARM) Climate Research Facility. (1993). *Updated hourly. Balloon-Borne Sounding System (SONDEWRPR). 2009 to 2017, Eastern North Atlantic (ENA/GRW) Graciosa Island, Azores, Portugal (C1)*. Compiled by C. Sivaraman, D. Holdridge, D. Troyan, J. Kyrouac, L. Riihimaki, R. Coulter, S. Giangrande, T. Shippert and T. Toto. Atmospheric Radiation Measurement (ARM) Climate Research Facility Data Archive: Oak Ridge, Tennessee, USA. Data set accessed 2017 at https://doi.org/10.5439/10214601

Atmospheric Radiation Measurement (ARM) Climate Research Facility. (2013). *Updated hourly. Surface Meteorological Instrumentation (MET). 2009–2010, 2013 to 2017, Eastern North Atlantic (ENA/GRW) Graciosa Island, Azores, Portugal (C1)*. Compiled by D. Holdridge and J. Kyrouac. Atmospheric Radiation Measurement (ARM) Climate Research Facility Data Archive: Oak Ridge, Tennessee, USA. Data set accessed 2017 at https://doi.org/10.5439/1025220

Atmospheric Radiation Measurement (ARM) Climate Research Facility. (2015). *Updated hourly. Active Remote Sensing of CLouds (ARSCL) product using Ka-band ARM Zenith Radars (ARSCLKAZRBND1KOLLIAS). 2009–2010, 2015 to 2017, Eastern North Atlantic (ENA/GRW) Graciosa Island, Azores, Portugal (C1)*. Compiled by K. Johnson, S. Giangrande and T. Toto. Atmospheric Radiation Measurement (ARM) Climate Research Facility Data Archive: Oak Ridge, Tennessee, USA. Data set accessed 2017 at https://doi.org/10.5439/1350630

Atmospheric Radiation Measurement (ARM) user facility. (2017). *Updated hourly. W-band Cloud Radar Active Remote Sensing of Cloud (ARSCLWACR1KOLLIAS). 2016-10-26 to 2017-03-31, ARM Mobile Facility (MAR) Hobart, AUS to Antarctic Coast - resupply ship Aurora Australis; AMF2 (M1)*. Compiled by S. Giangrande and K. Johnson. Oak Ridge, TN: Atmospheric Radiation Measurement (ARM) Climate Research Facility Data Archive. Data set accessed 2019-08-01 at https://doi.org/10.5439/1350613

Bretherton, C. S., Wood, R., George, R. C., Leon, D., Allen, G., & Zheng, X. (2010). Southeast Pacific stratocumulus clouds, precipitation and boundary layer structure sampled along 20°S during VOCALS-Rex. *Atmospheric Chemistry and Physics*, *10*(21), 10,639–10,654. https://doi.org/10.5194/cap-10-10639-2010

Clothiaux, E. E., Mace, G. G., Ackerman, T. P., Kane, T. J., Spinhirne, J. D., & Scott, V. S. (1998). An automated algorithm for detection of hydrometeor returns in micropulse Lidar data. *Journal of Atmospheric and Oceanic Technology*, *15*(4), 1035–1042. https://doi.org/10.1175/1520-0426(1998)015%3C1035:AAAFDO%3E2.0.CO;2

Eastman, R., Warren, S. G., & Hahn, C. J. (2011). Variations in cloud cover and cloud types over the ocean from surface observations, 1954-2008. *Journal of Climate*, *24*(22), 5914–5934. https://doi.org/10.1175/2011JCLI3972.1

Fletcher, J. K., Mason, S., & Jakob, C. (2016a). The climatology, meteorology and boundary layer structure of marine cold air outbreaks in both hemispheres. *Journal of Climate*, *29*(6), 1999–2014. https://doi.org/10.1175/JCLI-D-15-0268.1

Fletcher, J. K., Mason, S., & Jakob, C. (2016b). A climatology of clouds in marine cold air outbreaks in both hemispheres. *Journal of Climate*, *29*(18), 6677–6692. https://doi.org/10.1175/JCLI-D-15-0783.1

Gelaro, R., McCarty, W., Suárez, M. J., Todling, R., Molod, A., Takacs, L., et al. (2017). The Modern-Era Retrospective Analysis for Research and Applications, Version 2 (MERRA-2). *Journal of Climate*, *30*, 5419–5454. https://doi.org/10.1175/JCLI-D-16-0758.1

Gettelman, A., Callaghan, P., Larson, V. E., Zarzycki, C. M., Bacmeister, J. T., Lauritzen, P. H., et al. (2018). Regional climate simulations with the Community Earth System Model. *Journal of Advances in Modeling Earth Systems*, *10*, 1245–1265. https://doi.org/10.1002/2017MS001227

Ghate, V. P., Miller, M. A., Albrecht, B. A., & Fairall, C. W. (2015). Thermodynamic and radiative structure of stratocumulus-topped boundary layers. *Journal of the Atmospheric Sciences*, *72*(1), 430–451. https://doi.org/10.1175/JAS-D-13-0313.1

Giangrande, S. E., Wang, D., Bartholomew, M. J., Jensen, M. P., Mechem, D. B., Hardin, J. C., & Wood, R. (2019). Midlatitude oceanic cloud and precipitation properties as sampled by the ARM Eastern North Atlantic Observatory. *Journal of Geophysical Research: Atmospheres*, *124*, 4741–4760. https://doi.org/10.1029/2018JD029667

Hande, L. B., Siems, S. T., Manton, M. J., & Belusic, D. (2012). Observations of wind shear over the Southern Ocean. *Journal of Geophysical Research*, *117*, D12206. https://doi.org/10.1029/2012JD017488

Hartmann, D. L., Ockert-Bell, M. E., & Michelsen, M. L. (1992). The effect of cloud type on Earth's energy balance: Global analysis. *Journal of Climate*, *5*(11), 1281–1304. https://doi.org/10.1175/1520-0442(1992)005%3C1281:TEOCTO%3E2.0.CO;2

Haynes, J. M., Jakob, C., Rossow, W. B., Tselioudis, G., & Brown, J. (2011). Major characteristics of Southern Ocean cloud regimes and their effect on the energy budget. *Journal of Climate*, *24*(19), 5061–5080. https://doi.org/10.1175/2011JCLI4052.1

Kawai, H., Koshiro, T., & Webb, M. J. (2017). Interpretation of factors controlling low cloud cover and low cloud feedback using a unified predictive index. *Journal of Climate*, *30*(22), 9119–9131. https://doi.org/10.1175/JCLI-D-16-08251.1

Kawai, H., Yabu, S., Hagihara, Y., Koshiro, T., & Okamoto, H. (2015). Characteristics of the cloud top heights of marine boundary layer clouds and the frequency of marine fog over mid-latitudes. *Journal of the Meteorological Society of Japan*, *93*(6), 613–628. https://doi.org/10.2151/jmsj.2015-045

Kelleher, M. K., & Grise, K. M. (2019). Examining Southern Ocean cloud controlling factors on daily time scales and their connections to midlatitude weather systems. *Journal of Climate*, *32*(16), 5145–5160. https://doi.org/10.1175/JCLI-D-18-0840s1

Klein, S. A., Hall, A., Norris, J. R., & Pincus, R. (2017). Low-cloud feedbacks from cloud-controlling factors: A review. *Surveys in Geophysics*, *38*(6), 1307–1329. https://doi.org/10.1007/s10712-017-9433-3

Klein, S. A., & Hartmann, D. L. (1993). The seasonal cycle of low stratiform clouds. *Journal of Climate*, *6*(8), 1587–1606. https://doi.org/10.1175/1520-0442(1993)006%3C1587:TSCOLS%3E2.0.CO;2

Köhler, M., Ahlgrimm, M., & Beljaars, A. (2011). Unified treatment of dry convective and stratocumulus-topped boundary-layers in the ECMWF model. *Quarterly Journal of the Royal Meteorological Society*, *137*, 43–57. https://doi.org/10.1002/qj.713

Kuo, H.-C., & Schubert, W. H. (1988). Stability of cloud-topped boundary layers. *Quarterly Journal of the Royal Meteorological Society*, *114*(482), 887–916. https://doi.org/10.1002/qj.49711448204

Lamer, K., Naud, C. M., & Booth, J. F. (2020). Relationships between precipitation properties and large-scale conditions during subsidence at the ARM eastern North Atlantic observatory. *Journal of Geophysical Research: Atmospheres*, *125*, e2019JD031848. https://doi.org/10.1029/2019JD031848

Mace, G. G., & Protat, A. (2018). Clouds over the Southern Ocean as observed from the R/V investigator during CAPRICORN. Part I: cloud occurrence and phase partitioning. *Journal of Applied Meteorology and Climatology*, *57*(8), 1783–1803. https://doi.org/10.1175/JAMC-D-17-0194.1

Mace, G. G., Zhang, Q., Vaughan, M., Marchand, R., Sephens, G., Trepte, C., & Winker, D. (2009). A description of hydrometeor layer occurrence statistics derived from the first year of merged CloudSat and CALIPSO data. *Journal of Geophysical Research*, *114*, D00A26. https://doi.org/10.1029/2007JD009755

McCoy, I. L., Wood, R., & Fletcher, J. K. (2017). Identifying meteorological controls on open and closed mesoscale cellular convection associated with marine cold air outbreaks. *Journal of Geophysical Research: Atmospheres*, *122*, 11,678–11,702. https://doi.org/10.1002/2017JD027031

Myers, T. A., & Norris, J. R. (2013). Observational evidence that enhanced subsidence reduces subtropical marine boundary layer cloudiness. *Journal of Climate*, *26*(19), 7507–7524. https://doi.org/10.1175/JCLI-D-12-00736.1

Naud, C. M., Booth, J. F., & Del Genio, A. D. (2016). The relationship between boundary layer stability and cloud cover in the post-cold frontal region. *Journal of Climate*, *29*(22), 8129–8149. https://doi.org/10.1175/JCLI-D-15-0700.1

Naud, C. M., Booth, J. F., & Lamraoui, F. (2018). Post cold frontal clouds at the ARM eastern North Atlantic site: An examination of the relationship between large-scale environment and low-level cloud properties. *Journal of Geophysical Research: Atmospheres*, *123*, 12,117–12,132. https://doi.org/10.1029/2018JD029015

Norris, J. R. (1998). Low cloud type over the ocean from surface observations. Part I: relationship to surface meteorology and the vertical distribution of temperature and moisture. *Journal of Climate*, *11*, 369–382.

Protat, A., Schultz, E., Rikus, L., Sun, Z., Xiao, Y., & Keywood, M. (2017). Shipborne observations of the radiative effect of Southern Ocean clouds. *Journal of Geophysical Research: Atmospheres*, *122*, 318–328. https://doi.org/10.1002/2016JD026061

Rémillard, J., Kollias, P., Luke, E., & Wood, R. (2012). Marine boundary layer cloud observations in the Azores. *Journal of Climate*, *25*, 7381–7398. https://doi.org/10.1175/JCLI-D-11-00610.1

Rémillard, J., & Tselioudis, G. (2015). Climate regime variability over the Azores and its application to climate model evaluation. *Journal of Climate*, *28*(24), 9707–9720. https://doi.org/10.1175/JCLI-D-15-0066.1

Schneider, T., Kaul, C. M., & Pressel, K. G. (2019). Possible climate transitions from breakup of stratocumulus decks under greenhouse warming. *Nature Geoscience*, *12*(3), 163–167. https://doi.org/10.1038/s41561-019-0310-1

Wood, R. (2012). Stratocumulus clouds. *Monthly Weather Review*, *140*, 2373–2423. https://doi.org/10.1175/MWR-D-11-00121.1

Wood, R., & Bretherton, C. S. (2006). On the relationship between stratiform low cloud cover and lower-tropospheric stability. *Journal of Climate*, *19*, 6425–6432. https://doi.org/10.1175/JCLI3988.1

Wood, R., Wyant, M., Bretherton, C. S., Rémillard, J., Kollias, P., Fletcher, J., et al. (2015). Clouds, aerosols, and precipitation in the marine boundary layer: An ARM Mobile Facility deployment. *Bulletin of the American Meteorological Society*, *96*(3), 419–440. https://doi.org/10.1175/BAMS-D-13-00180.1

Zelinka, M. D., Myers, T. A., McCoy, D. T., Po-Chedley, S., Caldwell, P. M., Ceppi, P., et al. (2020). Causes of higher climate sensitivity in CMIP6 models. *Geophysical Research Letters*, *47*, e2019GL085782. https://doi.org/10.1029/2019GL085782

Zhao, M., Golaz, J. C., Held, I. M., Guo, H., Balaji, V., Benson, R., et al. (2018). The GFDL global atmosphere and land model AM4.0/LM4.0—Part II: Model description, sensitivity studies and tuning strategies. *Journal of Advances in Modeling Earth Systems*, *10*, 735–769. https://doi.org/10.1002/2017MS001209